ACS APPLIED MATERIALS & INTERFACES

Research Article

www.acsami.org

All-In-One Light-Tunable Borated Phosphors with Chemical and Luminescence Dynamical Control Resolution

Chun Che Lin,[†] Yun-Ping Liu,[‡] Zhi Ren Xiao,[§] Yin-Kuo Wang,[‡,∥] Bing-Ming Cheng,[⊥] and Ru-Shi Liu*[,†,#,○]

[†]Department of Chemistry, National Taiwan University, Taipei 106, Taiwan

[‡]Department of Physics, National Taiwan Normal University, Taipei 106, Taiwan

[§]Graduate Institute of Applied Physics, National Chengchi University, Taipei 116, Taiwan

[∥]Center for General Education and Department of Physics, National Taiwan Normal University, Taipei 106, Taiwan

[⊥]National Synchrotron Radiation Research Center, Hsinchu 300, Taiwan

[#]Department of Mechanical Engineering, National Taipei University of Technology, Taipei 10608, Taiwan

[○]Graduate Institute of Manufacturing Technology, National Taipei University of Technology, Taipei 10608, Taiwan

Supporting Information

ABSTRACT: Single-composition white-emitting phosphors with superior intrinsic properties upon excitation by ultraviolet light-emitting diodes are important constituents of next-generation light sources. Borate-based phosphors, such as $NaSrBO_3:Ce^{3+}$ and $NaCaBO_3:Ce^{3+}$, have stronger absorptions in the near-ultraviolet region as well as better chemical/physical stability than oxides. Energy transfer effects from sensitizer to activator caused by rare-earth ions are mainly found in the obtained photoluminescence spectra and lifetime. The interactive mechanisms of multiple dopants are ambiguous in most cases. We adjust the doping concentration in $NaSrBO_3$:RE (RE = Ce^{3+}, Tb^{3+}, Mn^{2+}) to study the energy transfer effects of Ce^{3+} to Tb^{3+} and Mn^{2+} by comparing the experimental data and theoretical calculation. The vacuum-ultraviolet experimental determination of the electronic energy levels for Ce^{3+} and Tb^{3+} in the borate host regarding the 4f−5d and 4f−4f configurations are described. Evaluation of the Ce^{3+}/Mn^{2+} intensity ratios as a function of Mn^{2+} concentration is based on the analysis of the luminescence dynamical process and fluorescence lifetime measurements. The results closely agree with those directly obtained from the emission spectra. Density functional calculations are performed using the generalized gradient approximation plus an on-site Coulombic interaction correction scheme to investigate the forbidden mechanism of interatomic energy transfer between the $NaSrBO_3:Ce^{3+}$ and $NaSrBO_3:Eu^{2+}$ systems. Results indicate that the $NaSrBO_3:Ce^{3+}$, Tb^{3+}, and Mn^{2+} phosphors can be used as a novel white-emitting component of UV radiation-excited devices.

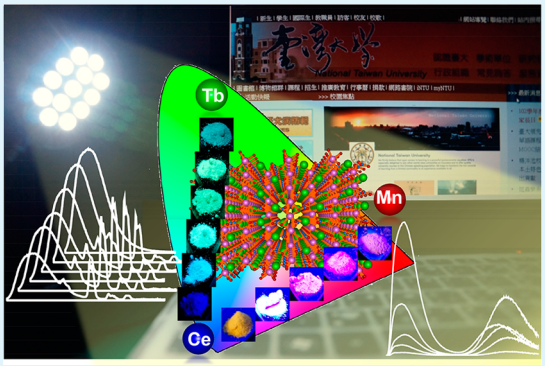

KEYWORDS: *white-emitting phosphors, energy transfer effects, DFT investigations, devices*

1. INTRODUCTION

Since the incorporation of Ce-doped yttrium aluminum garnet ($Y_3Al_5O_{12}:Ce^{3+}$; abbreviated as YAG:Ce^{3+}) as a vivacious emission layer for the fabrication of white light-emitting diodes (*w*-LEDs) by the Nichia Corporation, the performance of phosphor-converted LED (pc-LED) has been improved mainly by diversifying the components and encapsulation of the device as well as phosphor synthesis and architecture refinement.[1−3] Diverse approaches have been explored to enhance *w*-LED efficiency, such as by improving the chips, electric circuits, phosphors, and encapsulants.[4,5] Moreover, chromatic aberration and thermal quenching prevent the expansion of the most common *w*-LED composed of an InGaN-based blue diode and yellow YAG:Ce^{3+} phosphor.[6−8] An alternative way to overcome these difficulties is to combine ultraviolet (UV) LEDs (300 to 410 nm) with blue/green/red tricolor phosphors because these provide high color rendering indexes and excellent light output performances. However, the considerable reabsorption causes low luminescent efficiency, and the complicated design of multiple emitting components are rugged in this system.[9,10] In recent years, researchers have been developing single-composition white-emitting phosphors, which are excited by UV-LED to prevent the cross-color, instability of color temperature, and expensive cost problems. Even though the phosphor is an important component of the LED device, relatively scant studies have been conducted on the interactive

Received: March 3, 2014
Accepted: May 20, 2014
Published: May 20, 2014

   dx.doi.org/10.1021/am501232y | ACS Appl. Mater. Interfaces 2014, 6, 9160−9172

mechanism of the activators. Therefore, determination of the importance of the energy transfer effects in luminescent materials depends on experimental results and also theoretical calculations.[11] First, energy transfer from vicinal sensitizers has been considered to enhance or quench the improvement of the emission intensity in various activators. For instance, the broad emission band in the visible range of the transition metal Mn^{2+} originates from the d−d transition consisting of a forbidden transition and difficult excitation. For this reason, the distinct emission of Mn^{2+} ions is usually excited through energy transfer from the spectral overlap between the absorption band of Mn^{2+} ions and the emission band of promising sensitizer Eu^{2+} or Ce^{3+} ions in many hosts.[12−19] Second, considering the practical applications of LED devices, the excitation wavelength of the activators cannot match the requirements of the available chips. For example, the rigorously forbidden 4f−4f transitions of the Tb^{3+} absorption peaks in the near UV region are very weak. Some favorable ions such as Eu^{2+} and Ce^{3+}, whose electric dipole-allowed transition commonly engages beneficially in the UV- or blue-chip, can work as a helpful energy donor (D) in which the efficient energy transfer occurs between D and the energy acceptor (A).[20−27] According to Dexter's energy-transfer theory, the determination of efficiency principally depends on the spectral overlap between the emission spectra of the sensitizers and the absorption spectra of the activators.[28] Co-doped phosphor accompanied two kinds of transfer pathways: nonradiative and radiative. The nonradiative transfer mechanism is confusing because of the unknown multipolar interaction and exchange interaction.[11] Furthermore, the broad emission energy transition (5d → 4f) of the sensitizers, which is allowed by the Laporte parity selection rules, is deeply affected by the crystal field and the covalency of many inorganic hosts.[29]

Wu et al.[30] successfully synthesized a novel orthoborate ($NaSrBO_3$) that was crystallized in the monoclinic space group $P2_1/c$ consisting of the anisotropic polarizations of planar BO_3 groups, according to the powder X-ray diffraction data. This chemical composition has good quantum efficiency (QE), high color purity, low reaction temperature, and good stability when doped with rare-earth activators.[31−34] After our previous submission, Zhang et al.[35,36] reported the luminescence of single-doped phosphor $NaCaBO_3:Ce^{3+}$ and the color/chromaticity tenability of multidoped phosphor $NaCaBO_3:Ce^{3+}$, Tb^{3+}, and Mn^{2+} with the energy transfer processes of Ce^{3+} to Tb^{3+} and Mn^{2+}. Here, we demonstrate the parameters of borate crystallography ($NaSrBO_3$) in detail where Sr's are replaced by dopants. Moreover, we report the luminescent and energy transfer properties of the single-composition white-emitting phosphor $NaSrBO_3$:RE (RE = Ce^{3+}, Tb^{3+}, Mn^{2+}) which is of resonant type via a dipole−quadrupole mechanism while the transfer rate is strongly dependent on the critical distance based on the quenching and spectral overlap methods. In addition, the vacuum UV (VUV) spectra have been obtained for calculating the components of the 5d orbital of dopants. Except for the decay lifetime, the evidence of energy transfer has not been reported using the time-resolved photoluminescence approach in the $NaSr_{0.99-y}BO_3:Ce_{0.01}^{3+}$, Tb_y^{3+} phosphors. The relationship between distance and transfer rate of a sensitizer to an activator has been found out here. The transfer rate has been determined from the concentration of dopants favorably and compared with the result of CIE chromaticity coordinates. From related literature, Ce dopants in the $NaSrBO_3$ matrix receive high-energy photons and then transfer the resulting energy to Eu dopants while radiating low-energy photons. Particularly, the energy transfer of $Ce^{3+} \rightarrow Eu^{2+}$ is absent in the $NaSrBO_3$ system based on the theoretical calculation experiment. The as-prepared $NaSrBO_3$:RE (RE = Ce^{3+}, Tb^{3+}, Mn^{2+}) phosphors can generate white light for practical UV-LED devices. We have also constructed a significant model to explain a possible mechanism of interatomic energy transfer between rare-earth ions. From our study, it is clearly found that the $NaSrBO_3$:RE (RE = Ce^{3+}, Tb^{3+}, Mn^{2+}) phosphors have high emission intensity and better thermal stability as compared with the $NaCaBO_3$: RE (RE = Ce^{3+}, Tb^{3+}, Mn^{2+}) demonstrated by Zhang et al.[35]

2. EXPERIMENTAL SECTION

2.1. Materials and Synthesis. A series of borate-based $NaSr_{1-x-y-z}BO_3:Ce_x$, Tb_y, Mn_z compounds with versatile dopants were synthesized in one step by the solid-state reaction. The high-purity Na_2CO_3 (Crown Guaranteed Reagents, 99.7%), $SrCO_3$ (Aldrich, 99.99%), H_3BO_3 (Riedel-de Haën, 99.8%), CeO_2 (Aldrich, 99.995%), Tb_4O_7 (Aldrich, 99.99%), and Mn_2O_3 (Aldrich, 99%) were used as precursors in stoichiometric mixtures. Precise amounts of the starting materials were weighed out and ground in an agate mortar for 30 min to obtain homogeneous mixtures. The mixtures were placed in alumina crucibles and were then sintered at 850 °C for 8 h at a heating rate of 5 °C/min under a reducing atmosphere (N_2/H_2 = 95:5) in an electric tube furnace. After firing, the samples were gradually cooled to room temperature in the furnace. The products were crushed and prepared for measurements.

2.2. Characterization. The composition and phase purity of the products were identified using synchrotron X-ray diffraction (SXRD) patterns. A wavelength of λ = 0.774907 Å was recorded using a Debye−Scherrer camera installed at the BL01C2 beamline of the National Synchrotron Radiation Research Center (NSRRC) in Hsinchu, Taiwan. X-ray Rietveld refinement of the structural models and texture analysis were performed using the General Structure Analysis System (GSAS)[37] software. Photoluminescence excitation (PLE) and emission (PL) spectra were measured using the FluoroMax-3 and FluoroMax-P spectrophotometers equipped with a 150 W Xe lamp and a Hamamatsu R928 photomultiplier tube. The quantum efficiency (QE) was measured by the absolute method in HORIBA Jobin-Yvon spectrofluorimeters. An optical integrating sphere (diameter of 100 mm) showed a reflectance >99% over 400−1500 nm range (>95% within 250−2500 nm) in the device. The accessories were made from Teflon (rod and sample holders) or Spectralon (baffle). VUV PLE and PL spectra were obtained using a beamline BL03A at NSRRC. The PLE spectra were obtained by scanning a 6 m cylindrical grating (450 grooves/mm) monochromator, which has a spanning wavelength range of 85 to 350 nm. A CaF_2 plate with a cutoff wavelength at approximately 123 nm was used as a filter to remove the high-order light from the synchrotron. The PL spectra were evaluated with a 0.32 m monochromator and detected with a PMT in a photon-counting mode. Lifetime and time-resolved PL profiles were recorded at room temperature using an Edinburgh FLS920 spectrometer with a gated hydrogen arc lamp with a scatter solution to profile the instrument response function. Diffuse reflection spectra were obtained using a UV−vis spectrophotometer (Thermo Scientific evolution 220) attracted to an integral sphere. Drawings of the crystal structure were produced using a three-dimensional visualization system for electronic and structural analysis (VESTA).[38]

2.3. Computational Method. Density functional calculations were performed using the generalized gradient approximation (GGA-PBE) to investigate the electronic structures of the $NaSrBO_3$:Ce and $NaSrBO_3$:Eu systems. We calculated two systems separately because the orbitals on Ce and Eu atoms need not interact with each other in our model. We used the full-potential projector augmented wave (PAW)[39] method and the GGA with on-site Coulombic interaction correction (GGA+U),[40] which was implemented in the VASP code[41,42] to calculate the electronic structure and compare the result with the experimental data. The Ce and Eu 4f eletrons were

considered in the GGA+U scheme with U = 3.0 eV and exchange J = 0.9 eV. The crystal structure for calculations was based on the results determined by Wu et al.[30] To simulate the 6.25% (1/16) of Ce- and Eu-doped systems, a 2 × 1 × 2 supercell was considered wherein one of the Sr was replaced by Ce or Eu.

2.4. Package. First, the as-synthesized borated samples were finely pulverized and sieved for an encapsulation. Second, the phosphors were blended with thermally curable silicone resin (OE-6630B, Dow Corning), and then the hardener (OE-6630A) was added to the mixture. The weight percentage of the phosphor was 10−30 wt % in the epoxy resin. The mixture was dropped onto a UV LED chip (spectrum peak λ = 365 nm, optical power 2 mW). Finally, the chip was heated through a two-step thermal curing process at 100 °C for 1 h and then at 150 °C for 2 h in an oven.

3. RESULTS AND DISCUSSION

3.1. Structural Refinement and Crystal Parameters. The composition, phase purity, and atomic position of the as-synthesized samples were determined using GSAS and VESTA software. Figure 1 shows the Rietveld analysis of the

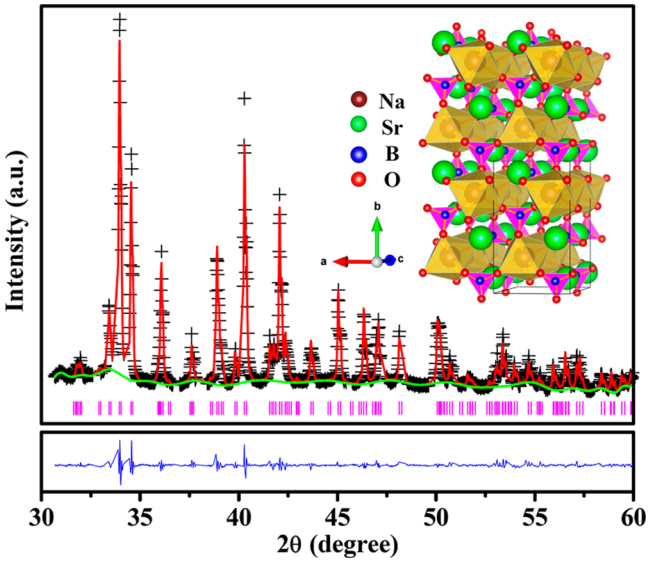

Figure 1. Rietveld refinement of the experimental (crosses) and calculated (solid line) SXRD patterns of the $NaSr_{0.99}BO_3$:$Ce_{0.01}$. Purple vertical lines represent the position of Bragg reflection. The difference profile is plotted on the same scale at the bottom. Structure refinement shows the crystal structure of $NaSrBO_3$ views in the *ac* direction (inset).

$NaSr_{0.99}BO_3$:$Ce_{0.01}$ SXRD patterns. The doped-product crystallizes as a monoclinic structure with a space group of $P2_1/c$ and a = 5.32839(9) Å, b = 9.27904(15) Å, and c = 6.07417(14) Å. All of the parameters of crystallography and observed peaks are consistent with the reflection condition, lattice constants, and cell volume (Table 1). The results demonstrate that no recognized byproduct phase is observed in a series of samples even under various conditions. The codoped Ce^{3+}, Tb^{3+}, and Mn^{2+} ions also did not cause any significant changes in the obtained samples, regardless of the concentrations of the dopants. Hence, similar results are not shown in the article. The inset illustrates the schematic representation of the structural skeleton of $NaSrBO_3$ plotted according to the refinement data. The foundational structure consists of isolated planar $[BO_3]^{3-}$ anionic groups distributed in a parallel fashion along two directions. Additionally, Figure 2a presents the nine-coordinated Sr^{2+} in one crystallographic structure and six-coordinated

Table 1. Crystallographic Data of $NaSr_{0.99}BO_3$:$Ce_{0.01}$ Derived from Rietveld Refinement of the SXRD Patterns at Room Temperature[a]

$NaSr_{0.99}BO_3$:$Ce_{0.01}$					
atoms	x/a	y/b	z/c	S.O.F.	U_{iso} × 100 (Å^2)
Sr(1)	0.242 726	0.413 584	0.222 544	0.99	3.61
Na(1)	0.265 382	0.762 744	0.032 741	1.10	8.19
O(1)	0.018 970	0.663 724	0.199 712	0.91	0.36
O(2)	−0.407 279	0.665 128	0.402 537	1.06	9.80
O(3)	0.298 511	0.934 916	0.307 579	1.04	0.93
B(1)	−0.331 457	0.611 297	0.274 359	0.79	8.56
Ce(1)	0.707 720	−8.581 388	8.985 068	0.01	8.93

[a]Crystal structure: monoclinic. Space group: $P2_1/c$. a = 5.32839(9) Å, b = 9.27904(15) Å, c = 6.07417(14) Å, cell volume = 295.194(10) Å^3. χ^2 = 2.99, R_p = 2.71%, R_{wp} = 3.97%.

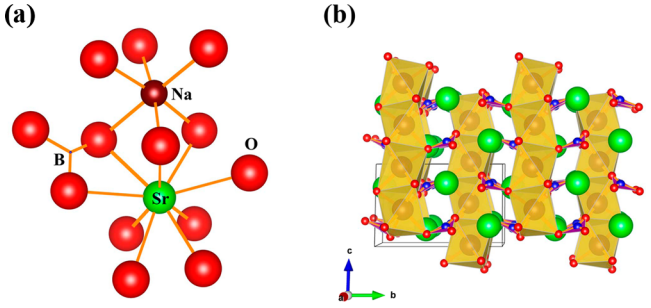

Figure 2. (a) Coordination environments of the metal ion sites in the $NaSrBO_3$ structure. The metal ions are linked with corner-sharing oxygen atoms in the heteropolyhedral coordination network. (b) View of 2 × 2 × 2 unit cells along the [100] direction.

Na^+ with an octahedral polyhedron in the $NaSrBO_3$ structure. Figure 2b portrays the structure of 2 × 2 × 2 unit cells highlighted by the tilted $[NaO_6]^{11-}$ polyhedrons connected with planar $[BO_3]^{3-}$ groups, which results in a lower symmetry space group of this material. Based on the above analysis and the effective ionic radii between the cations and rare-earth ions with different coordination numbers (Table 2),[43] these rare-earth ions can be substitutes for Sr^{2+} ions in the host structure. Therefore, no impurity phase after different ions are doped in the system is observed.

Table 2. Ionic Radii (Å) of Na^+, Sr^{2+}, B^{3+}, and RE (RE = Ce^{3+}, Tb^{3+}, Mn^{2+}) Using the Given Coordination Number (CN)

atoms	CN		ionic radii (Å)	
Na^+	6		1.020	
Sr^{2+}	9		1.310	
B^{3+}	6		0.270	
Ce^{3+}	9	6	1.196	1.010
Tb^{3+}	9	6	1.095	0.923
Mn^{2+}	8	6	0.960	0.830

3.2. PL Properties of Ce^{3+}-, Tb^{3+}-, and Mn^{2+}-doped $NaSrBO_3$. Upon excitation by UV−visible sources, the $NaSrBO_3$:Ce^{3+}, $NaSrBO_3$:Tb^{3+}, and $NaSrBO_3$:Mn^{2+} samples exhibit pure blue, green, and red luminescence to the naked eye, respectively. The doping concentrations of Ce^{3+}, Tb^{3+}, and Mn^{2+} in the $NaSrBO_3$ host structure were optimized at 1 atom %, 7 atom %, and 5 atom % in the synthetic procedure,

dx.doi.org/10.1021/am501232y | ACS Appl. Mater. Interfaces 2014, 6, 9160−9172

respectively. Figure 3a illustrates the PLE and PL spectra of the Ce^{3+}-doped $NaSrBO_3$ sample in which the PLE spectrum was

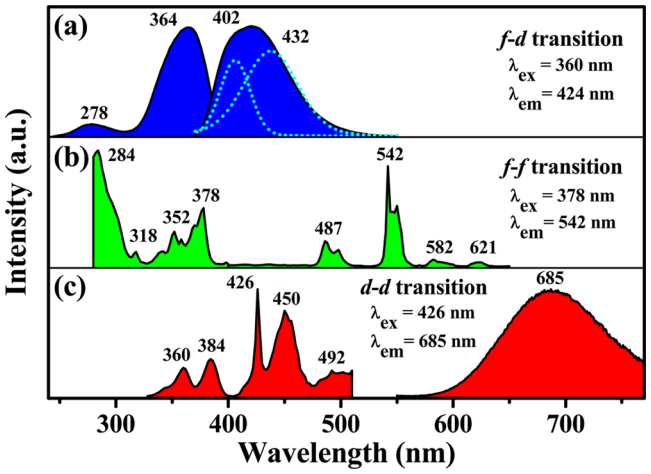

Figure 3. PL excitation (left) and emission (right) spectra of the (a) $NaSr_{0.99}BO_3:Ce_{0.01}^{3+}$, (b) $NaSr_{0.93}BO_3:Tb_{0.07}^{3+}$, and (c) $NaSr_{0.95}BO_3:Mn_{0.05}^{2+}$ samples. The corresponding monitoring wavelengths are also given.

monitored at 424 nm and the PL was excited at 360 nm. The PLE spectrum shows two distinct excitation bands at 278 and 364 nm; the late band is consistent with the 365 nm UV-LED chips. The dominant band (364 nm) is assigned to the 4f–5d transition of Ce^{3+}, which is an excellent sensitizer for the f–f forbidden transition of activators in multiple electronic configurations. The corresponding emission spectrum (λ_{ex} = 360 nm) shows an asymmetric band that extends from 370 to 510 nm with a maximum at approximately 424 nm, which is known to be the typical transition from the 5d excited state to the $^2F_{5/2}$ and $^2F_{7/2}$ ground states. Through Gaussian deconvolution, the broad emission band can be decomposed into two Gaussian profiles (the blue dashed lines) with peaks centered at 402 nm (24 876 cm^{-1}) and 432 nm (23 148 cm^{-1}) with an energy difference of approximately 1728 cm^{-1}, which is consistent with the theoretical value of 2000 cm^{-1}.[11,24,44] However, the normalized PL spectra of the $NaSr_{1-}BO_3:Ce_x^{3+}$ (x = 0.01 to 0.10) materials were decomposed into Gaussian contributions in the Supporting Information (Figure S1) wherein the arrows illustrate the energy shift and change in relative intensity with increased values of x. The main reason causes the red shift in the emission spectra due to the reabsorption effect, which is the overlap of excitation and emission bands at high Ce^{3+} concentrations.[45]

The representative 4f–4f intraconfiguration forbidden transition of the Tb^{3+}-doped $NaSrBO_3$ sample is presented in Figure 3b. The $4f^8$ electronic configuration is on the $^7F_6$ level of the Tb^{3+} ground state, and it has the high-spin ^9D_J and the low-spin ^7D_J states in $4f^75d^1$ excitation levels. The excitation spectrum consists of a strong band at 240 nm (Figure 4c) and some narrow lines at 280 to 450 nm that are assigned to the spin-allowed states ($\Delta S = 0$) of the $4f^8 \rightarrow 4f^75d^1$ transition and f–f forbidden transition ($\Delta S = \pm 1$), respectively. The formula $\Delta E^{Tb,Ce} = E(Tb,A) - E(Ce,A)$ shows that the energy difference between the first f–d transition of the Tb^{3+} ions (287 nm, 34 843 cm^{-1}) and Ce^{3+} ions (210 nm, 47 619 cm^{-1}) (Figure 4a) is 12 776 cm^{-1}.[44] Consequently, the result is close to the average value of 13 200 cm^{-1} for the spin-allowed f–d transition of the Tb^{3+} ions. The energy difference between the spin-allowed (f–d) transition and spin-forbidden (f–f) transition is 6802 cm^{-1} [ΔE = 35 211 cm^{-1} (284 nm) − 28 409 cm^{-1} (352 nm)], which is consistent with the previous reported value of 6300 cm^{-1}.[46] Except for the above observation, several excitation bands from $^7F_6$ to $^5F_{5,4}$, $^5H_{7-4}$, $^5D_{1,0}$, $^5L_{10-7}$, $^5G_{6-2}$, and $^5D_{2-3}$ levels are observed because of the $4f^8$ electronic configuration. Furthermore, the PL spectrum under the excitation of 378 nm displays lower emission-state $^5D_4 \rightarrow {}^7F_J$ (J = 3, 4, 5, 6) transitions at 487, 542, 582, and 621 nm that correspond to the typical 4f → 4f intraconfiguration forbidden transitions of Tb^{3+} ions. The major emission peak that is centered at 542 nm corresponds to the $^5D_4$–$^7F_5$ transition, which can be elucidated using the reduced matrix elements at J = 5 and the Judd–Ofelt theory.[47,48] The phosphor emits approximately green luminescence with a relaxation of the $^5D_3$ level because the nonradiative

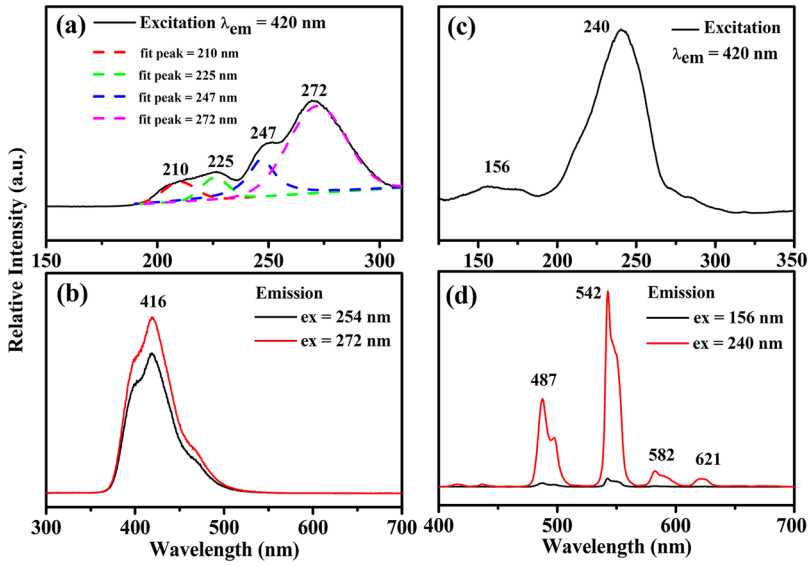

Figure 4. VUV-PLE and PL spectra of (a, b) $NaSr_{0.99}BO_3:Ce_{0.01}^{3+}$ (PLE monitored at 420 nm; PL excited at 254 and 272 nm) and (c, d) $NaSr_{0.93}BO_3:Tb_{0.07}^{3+}$ (PLE monitored at 542 nm; PL excited at 156 and 240 nm).

cross-relaxation mechanism favors a greater occupancy of $^5D_4$ level at the expense of the $^5D_3$ level: $Tb^{3+}(^5D_3) + Tb^{3+}(^7F_6) \rightarrow Tb^{3+}(^5D_4) + Tb^{3+}(^7F_0)$. This effect is responsible for the enhancement of the green emissions by the transitions from the highly populated $^5D_4$ level when the Tb^{3+} concentration is increased.[49,50]

According to the literature, the broad emission band (400 to 750 nm) of Mn^{2+}-doped luminescent materials is ascribed to the $^4T_1(^4G) \rightarrow {}^6A_1(^6S)$ transition within the 3d shell where the electrons are strongly coupled to the lattice vibration as well as significantly affected by the strength of the crystal field and coordination numbers. The Mn^{2+} ions with different crystal field strengths can adjust the emission color from blue/green (weak crystal field) to orange/red (strong crystal field).[11,51,52] Therefore, because of its strong crystal field, the Mn^{2+}-doped $NaSrBO_3$ phosphor shows red emission (Figure 3c). Mn^{2+} ions also substituted the nine-coordinate Sr^{2+} sites in the host lattice successfully. Furthermore, the PLE spectrum consists of several weak bands in the UV and visible locations because of the spin-forbidden transitions of the $3d^5$ electronic configurations of Mn^{2+} ions. On the basis of the Orgel diagram,[53] the peaks center at 360, 384, 426, 450, and 492 nm because of the transitions from the ground-state level $^6A_1(^6S)$ to the $^4E(^4D)$, $^4T_2(^4D)$, $[^4A_1(^4G), {}^4E(^4G)]$, $^4T_2(^4G)$, and $^4T_1(^4G)$ excited-state levels, respectively. Figure 3 shows a significant spectral overlap between the emission of Ce^{3+} and the excitation of Tb^{3+} and Mn^{2+}; therefore, effective energy transfer from Ce^{3+} to Tb^{3+} and Mn^{2+} are expected for the codoped samples.

The reflectance spectra of the $NaSrBO_3$ host, $NaSr_{0.99}BO_3:Ce_{0.01}{}^{3+}$, $NaSr_{0.98}BO_3:Ce_{0.01}{}^{3+}$, $Tb_{0.01}{}^{3+}$, and $NaSr_{0.98}BO_3:Ce_{0.01}{}^{3+}$, $Mn_{0.01}{}^{2+}$ samples are shown in Figure S2. No host absorption/emission in the *n*-UV region is observed because the $NaSrBO_3$ host absorbs energy below the 200 nm region. Nevertheless, the $NaSr_{0.99}BO_3:Ce_{0.01}{}^{3+}$ and $NaSr_{0.98}BO_3:Ce_{0.01}{}^{3+}$, $Tb_{0.01}{}^{3+}$ phosphors exhibit three similar absorption bands with maxima at 240, 310, and 389 nm in the 200 to 450 nm UV region. These are assigned to the f−d absorption bands of the Ce^{3+} ions. As Mn^{2+} ions are introduced into the borate host, two obscure absorption bands are found at 300 and 384 nm attributed to the complicated excited-state levels of the spin-forbidden transitions of Mn^{2+} ions. All of the phenomena are also consistent with the PLE spectra of the three samples shown Figure 3, which suggest that the $NaSrBO_3:Ce^{3+}$, Tb^{3+} and $NaSrBO_3:Ce^{3+}$, Mn^{2+} samples have an expansive and strong absorption range that matches well with *n*-UV chips, thereby making them good phosphor candidates for *w*-LED's.

The VUV-PLE and PL spectra of the $NaSr_{0.99}BO_3:Ce_{0.01}{}^{3+}$ and $NaSr_{0.93}BO_3:Tb_{0.07}{}^{3+}$ samples are presented in Figure 4. The excitation spectrum of the Ce^{3+} ion (Figure 4a) directly shows the energy state of the 5d level by Gaussian deconvolution. This can also be used as a strategy to explore the f−d transitions of other rare-earth ions in the same host lattice sites because of the similarity of the crystal field effects on the 5d states of different rare-earth ions. In addition, the $[Xe]4f^{n-1}5d^1$ energy configuration can be estimated by the following empirical eqs 1 and 2:[46]

$$E_{abs}(n, Q, A) = E_{Afree}(n, Q) - D(Q, A) \quad (1)$$

$$E_{em}(n, Q, A) = E_{Afree}(n, Q) - D(Q, A) - \Delta S(Q, A) \quad (2)$$

where $E_{Afree}(n,Q)$ is a constant of each Ce^{3+} free ion which approaches the energy of the first fd transition; $D(Q,A)$ and $\Delta S(Q,A)$ are the red shift and Stokes shift in the borate compound, respectively. The effect of the energy of the $[Xe]5d^1$ configuration of Ce^{3+} in the borate compounds has not been reported. The components of the 5d orbital, crystal field splitting, 5d barycenter, emission band, and Stokes shift are recorded in Table 3.[54] Furthermore, the centroid shift (ε_c),

Table 3. Spectroscopic Data of the $[Xe]5d^1$ Configuration of Ce^{3+} in Inorganic Compound

sample	$NaSrBO_3:Ce^{3+}$
first 5d component (nm)	360
second 5d component (nm)	272
third 5d component (nm)	247
fourth 5d component (nm)	225
fifth 5d component (nm)	210
crystal field splitting (10^3 cm^{-1})	19.8
5d barycenter (10^3 cm^{-1})	40.5
emission band (nm)	402, 432
Stokes shift (10^3 cm^{-1})	2.901

which is the energy difference between the 5d configuration of Ce^{3+} as a free ion and in the $NaSrBO_3$ compound is 10.745×10^3 cm^{-1}. The semiquantitative centroid shift (ε_c) is calculated depending on the matrix's average electronegativity values using the following eq 3:[55]

$$\varepsilon_c = 1.79 \times 10^{13} \sum_{i=1}^{N} \frac{\alpha_{sp}^{i}}{(R_i - 0.6\Delta R)^6} \quad (3)$$

where $\alpha_{sp}{}^{i}$ ($\alpha_{sp}{}^{o} = 0.33 + 4.8/\chi_{av}{}^2$) is the spectroscopic polarizability of an anion ligand (i), χ_{av} is the weighted average of the electronegativity of the cations in the oxide, R_i is the distance between Ce^{3+} and the anion ligands (i) in the unrelaxed lattice, and ΔR is the difference in the ionic radius between the Ce^{3+} ion and the substituted cation. For example, $\chi_{NaSrBO3} = (1\chi_{Na} + 2\chi_{Sr} + 3\chi_B)/6 = 1.49$, $\alpha_{sp}{}^{o} = 2.49$, $R_i = 257.9-283.4$ pm, and $\Delta R = 11.4$ pm. From previous reports using eq 3, the centroid shift (ε_c) values of some borate compounds are between 8.730×10^3 cm^{-1} and 12.730×10^3 cm^{-1}. This result also indicates that the experimental result is consistent with the calculated data. In Figure 4c, the only broad excitation line is observed from 180 to 300 nm attributed to the $4f^8 \rightarrow 4f^7 5d^1$ transition of the Tb^{3+} ions. The PL spectra (Figure 4b and d) of the $NaSr_{0.99}BO_3:Ce_{0.01}{}^{3+}$ and $NaSr_{0.93}BO_3:Tb_{0.07}{}^{3+}$ phosphors with optimized composition under VUV radiation are similar to that in Figure 3 except for the difference of the relative intensity.

3.3. Energy Transfer between Luminescent Centers.

The energy transfer mechanism is important in generating white light and in improving the QE of single-composition white-emitting phosphors. Figure 5a displays the PL spectra of $NaSr_{0.99-y}BO_3:Ce_{0.01}{}^{3+}$, $Tb_y{}^{3+}$ phosphors based on Tb^{3+} doping content (y). The emission spectrum appears not only as a blue band of Ce^{3+} ions but also as an intense green band of Tb^{3+} ions under excitation by 360 nm radiation. By increasing the Tb^{3+} concentration (y), the green emission of Tb^{3+} ions also increases gradually while the blue emission of Ce^{3+} ions decreases. This observation implicates that the resonance type energy transfer from Ce^{3+} to Tb^{3+} ions can be expected to occur in the $NaSrBO_3$ host lattice. Moreover, other possible

dx.doi.org/10.1021/am501232y | ACS Appl. Mater. Interfaces 2014, 6, 9160−9172

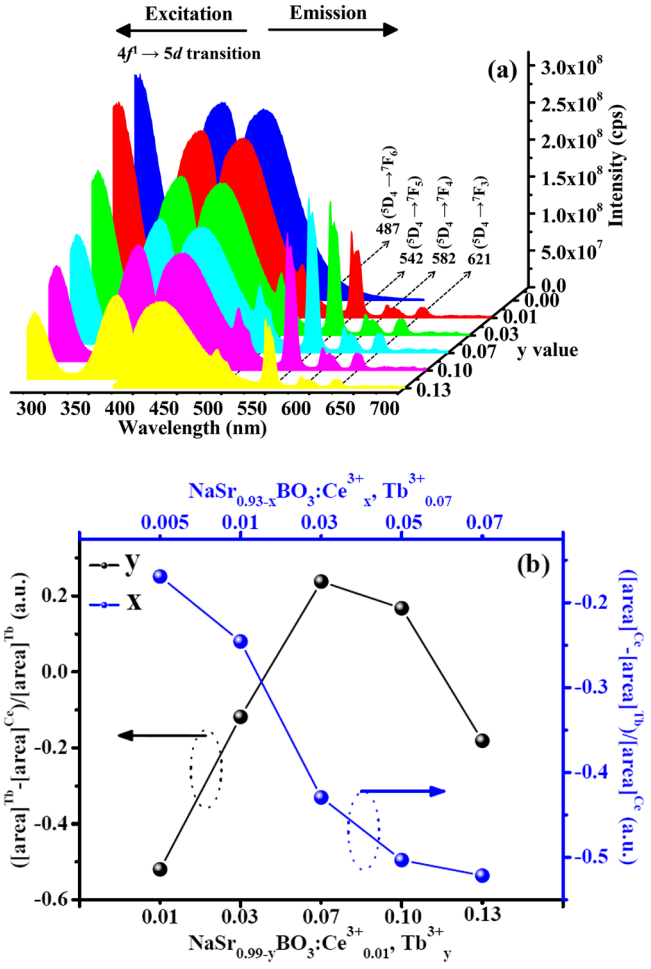

Figure 5. (a) PL excitation (left) and emission (right) spectra of the $NaSr_{0.99-y}BO_3:Ce_{0.01}^{3+}$, Tb_y^{3+} phosphors on Tb^{3+} doping content (y). (b) Dependence of Ce^{3+} and Tb^{3+} emission on the activator concentration for the $NaSr_{0.99-y}BO_3:Ce_{0.01}^{3+}$, Tb_y^{3+} and $NaSr_{0.93-x}BO_3:Ce_x^{3+}$, $Tb_{0.07}^{3+}$ phosphors.

mechanisms of energy transfer are possible in this system; for example, the radiation transitions of Tb^{3+} ions may directly excite the neighboring Ce^{3+} ions. The PLE and PL spectra of the $NaSr_{0.93-x}BO_3:Ce_x^{3+}$, $Tb_{0.07}^{3+}$ phosphors with various Ce^{3+} doping concentration (x) are shown in Figure S3. The results are contradictory to the $Tb^{3+} \rightarrow Ce^{3+}$ energy transfer effect. Figure 5b illuminates the dependence of the integral emission areas of both the f–f transition (480–650 nm) and f–d transition (370–480 nm) on the concentrations of the activators for the $NaSr_{0.99-y}BO_3:Ce_{0.01}^{3+}$, Tb_y^{3+} and $NaSr_{0.93-x}BO_3:Ce_x^{3+}$, $Tb_{0.07}^{3+}$ phosphors. We propose the accurate calculation of the relative ratio of Ce^{3+} and Tb^{3+} using the following eq 4:

$$A_1 = [(\text{area})^{A} - (\text{area})^{S}]/(\text{area})^{A_0} \quad (4)$$

where A_1 is the percentage of change of A (activator), $(\text{area})^{A}$ and $(\text{area})^{S}$ are the integral emission area of A or S (sensitizer) with a codoping matrix in the same host lattice, and $(\text{area})^{A_0}$ is the integral emission area of A as a single-doping matrix. For the $NaSr_{0.99-y}BO_3:Ce_{0.01}^{3+}$, Tb_y^{3+} series (black line), the emission area of the Tb^{3+} ions increases remarkably because of the enhancement caused by the energy transfer effect ($Ce^{3+} \rightarrow Tb^{3+}$) at $y = 0.07$. By contrast, the emission area decreases progressively when $y > 0.07$ because of the internal concentration quenching effect of Tb^{3+}–Tb^{3+} clusters.[56,57] In the $NaSr_{0.93-x}BO_3:Ce_x^{3+}$, $Tb_{0.07}^{3+}$ series (blue line), the emission area of the Ce^{3+} ions decreases significantly because the Tb^{3+} ion cannot be used as a sensitizer that transfers its energy to the Ce^{3+} activator. The Tb^{3+} ion exhibits green light as an activator. The chromatic lighting can be adopted in accordance with the A_1 value in the $NaSr_{0.99-y}BO_3:Ce_{0.01}^{3+}$, Tb_y^{3+} series, such as blue (negative A_1) and green (positive A_1); the digital images are shown in Figure S7a.

The luminescence dynamics can be thoroughly investigated using the PL decay curve, time-resolved PL, the lifetime calculation, and the energy transfer efficiency because these suggest the interaction of the activators. The decay curve of the $NaSr_{0.99}BO_3:Ce_{0.01}^{3+}$ phosphor fits a single-exponential function $[I = I_0 \exp(-t/\tau)]$ with a lifetime of approximately 208.5 ns (Figure 6). Additionally, the decay curves of the NaS-

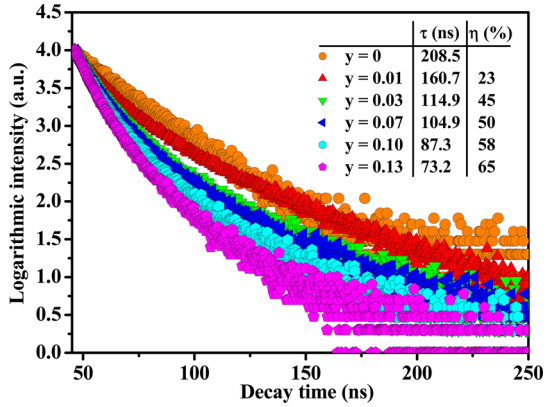

Figure 6. PL decay curves of Ce^{3+} in $NaSr_{0.99-y}BO_3:Ce_{0.01}^{3+}$, Tb_y^{3+} phosphors (excited at 360 nm, monitored at 424 nm). The inset shows the lifetimes of Ce^{3+} and the energy transfer efficiency from Ce^{3+} to Tb^{3+}.

$r_{0.99-y}BO_3:Ce_{0.01}^{3+}$, Tb_y^{3+} (y = 0.01 to 0.13) phosphors show nonexponential curves that indicate that the introduction of Tb^{3+} ions changes the fluorescence dynamics of the Ce^{3+} ions. This result also confirms the existence of clusters with different exponential decay rates, such as the Ce–Ce, Tb–Tb, and Ce–Tb clusters. It also indicates that several energy transfer pathways between Ce and Tb activators result in different exponential decay rates. The decay course of these compounds is evaluated by average lifetime.[24] The average luminescent lifetime of Ce^{3+} ions as a function of different Tb^{3+} concentration is calculated using the following eqs 5 and 6:[44,58]

$$\tau = \frac{\int_0^\infty I(t)t \, dt}{\int_0^\infty I(t) \, dt} \quad (5)$$

where τ is the average lifetime and $I(t)$ is the intensity at time t.

$$\tau = (A_1\tau_1^2 + A_2\tau_2^2)/(A_1\tau_1 + A_2\tau_2) \quad (6)$$

where τ is the average lifetime, τ_1 and τ_2 are the lifetimes, and A_1 and A_2 are the constants. According to eqs 5 and 6, the tendency of the average lifetime is very similar among the series of samples (Figure 6). The decay lifetime of Ce^{3+} ions decreases monotonically with increased Tb^{3+} concentration, which strongly supports the energy transfer from Ce^{3+} to Tb^{3+}. The energy transfer efficiency (η_T) from Ce^{3+} to Tb^{3+} can be calculated using the following eq 7:[59]

dx.doi.org/10.1021/am501232y | ACS Appl. Mater. Interfaces 2014, 6, 9160–9172

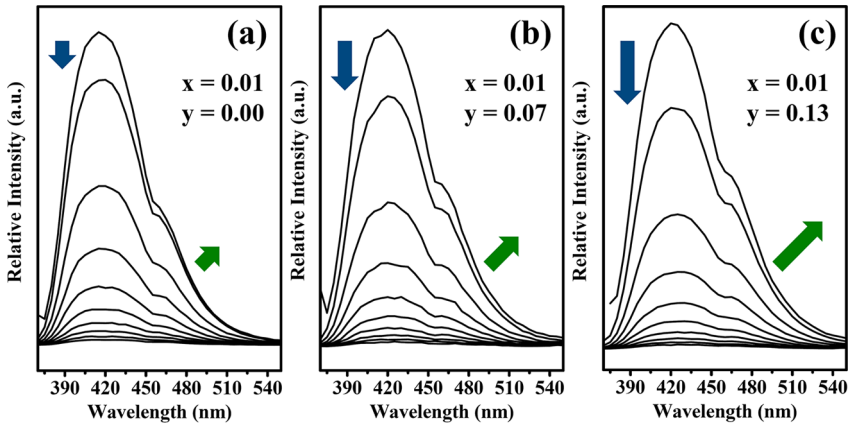

Figure 7. Time-resolved PL of Ce^{3+} in $NaSr_{0.99-y}BO_3:Ce_{0.01}{}^{3+}$, $Tb_y{}^{3+}$ phosphors. (a) y = 0, (b) y = 0.07, and (c) y = 0.13; samples at room temperature, excited at 360 nm and recorded with delay times of up to 220 ns. The arrows show the change of the intensity as a function of Tb^{3+} concentration.

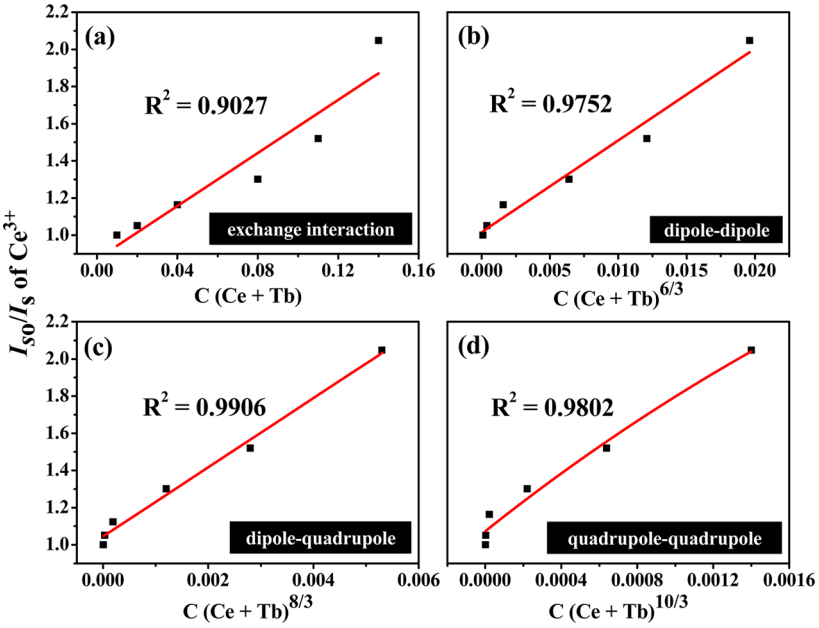

Figure 8. Dependence of I_{so}/I_s of Ce^{3+} ions on (a) C (Ce + Tb), (b) C (Ce + Tb)$^{6/3}$, (c) C (Ce + Tb)$^{8/3}$, and (d) C (Ce + Tb)$^{10/3}$.

$$\eta_T = 1 - \frac{\tau_S}{\tau_{S0}} \quad (7)$$

where τ_{S0} and τ_S are the lifetimes of Ce^{3+} in both the absence and the presence of Tb^{3+}, respectively. Considering the average lifetimes and eq 7, the maximum energy-transfer efficiency ($Ce^{3+} \rightarrow Tb^{3+}$) is estimated to be 65% at y = 0.13 (Figure 6 inset). The decay lifetime has been applied previously to prove the energy transfer process of the codoping materials. Evidence of energy transfer using the time-resolved PL approach in $NaSr_{0.99-y}BO_3:Ce_{0.01}{}^{3+}$, $Tb_y{}^{3+}$ phosphors has not been reported. The rapid reduction in Ce^{3+} emission (blue arrow) and gradual increment in Tb^{3+} emission (green arrow) are clearly observed with increased Tb^{3+} concentration (y value; Figure 7). The phenomenon is ascribed to the energy transfer from Ce^{3+} to Tb^{3+} at the release and acquirement of energy, respectively. Moreover, the spectral change of the $NaSr_{0.92}BO_3:Ce_{0.01}{}^{3+}$, $Tb_{0.07}{}^{3+}$ sample directly shows the energy transfer effect (Figure S4). Therefore, the time-resolved PL technique can be employed extensively to understand the luminescence dynamics of the other systems.

Three principal interactions may result in energy transfer from a sensitizer to an activator: radiative transfer, exchange interaction, and electric multipolar interaction. The occurrence of radiative transfer in the f–f absorption spectra of Tb^{3+} ions is responsible for the invariant emission intensity of Ce^{3+} ions and can be ignored. Given the distance between the donor and acceptor orbitals or necessary energies for the exchange of the reducing ions, the exchange interaction is constrained for energy transfer of the borate system. In preliminary speculations, the energy transfer of the $NaSrBO_3$:RE (RE = Ce^{3+}, Tb^{3+}) system proceeds through an electric multipolar interaction. In accordance with Dexter's energy transfer pronouncements of multipolar interaction and the Reisfeld approximation, the following relation can be expressed using eq 8:[28,60]

$$\frac{\eta_0}{\eta_S} \doteq \frac{I_{S0}}{I_S} \propto C^{n/3}_{Ce^{3+}+Tb^{3+}} \quad (8)$$

where η_0 is the intrinsic luminescence QE of Ce^{3+} and η_S is the luminescence QE of Ce^{3+} in the presence of Tb^{3+}. The value of η_0/η_S can be approximated by the luminescence intensity ratio (I_{S0}/I_S). C is the total concentration of Ce^{3+} and Tb^{3+} ions, and n is the interaction of the energy transfer mechanism. The relationship of (I_{S0}/I_S) vs $C_{Ce^{3+}+Tb^{3+}}{}^{n/3}$ is plotted in Figure 8, where n = 3, 6, 8, and 10 for the exchange, dipole−dipole (dd), dipole−quadrupole (dq), and quadrupole−quadrupole (qq) interactions, respectively. According to the optimal fitting factors ($R^2 \doteqdot 1$) of linear relationship, the energy transfer ($Ce^{3+} \rightarrow Tb^{3+}$) of the $NaSrBO_3$:Ce^{3+}, Tb^{3+} system occurs predominantly via the dipole−quadrupole (dq) interaction (Figure 8c).

The effective energy transfer from Ce^{3+} to Mn^{2+} is expected because of the significant spectral overlap between the emission of Ce^{3+} and the excitation of Mn^{2+} (Figure 3). Consequently, the PL spectra are composed of the blue and red emission bands, which are assigned to the distinctive f−d allowed transition of Ce^{3+} and the d−d forbidden transition of Mn^{2+} in the $NaSr_{0.99-z}BO_3$:$Ce_{0.01}{}^{3+}$, $Mn_z{}^{2+}$ samples, respectively (Figure 9). The variation of both emission bands (Ce^{3+} and Mn^{2+}) is

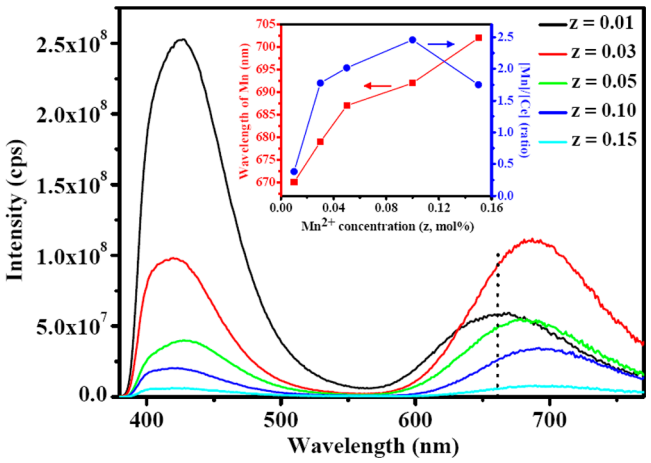

Figure 9. Dependence of PL spectra of Ce^{3+} and Mn^{2+} in the $NaSr_{0.99-z}BO_3$:$Ce_{0.01}{}^{3+}$, $Mn_z{}^{2+}$ samples on the Mn^{2+} doping concentrations (z = 0.01−0.15). The inset shows the variation in emission wavelengths (nm) of Mn^{2+} ions and the ratio of emission area ([Mn]/[Ce]) with increased Mn^{2+}-doping concentrations from 0.01 to 0.15.

observed when the Mn^{2+}-doping concentrations are increased from 0.01 to 0.15. This result supports the energy transfer from Ce^{3+} to Mn^{2+} ($ET_{Ce\rightarrow Mn}$) and the red-shift of Mn^{2+} emissions as the z value increases. This observation may be attributed to the significant dispersion of sizes ($^{[9]}r(Sr^{2+})$ = 1.31 Å) caused by a larger crystal field splitting of Mn^{2+} 3d energy levels as a result of size mismatch; the Mn dopant ($^{[8]}r(Mn^{2+})$ = 0.96 Å) is slightly smaller than the Sr^{2+} ions. The capacity of the red shift of Mn^{2+} emissions and the ratio of integral emission areas (red/blue) are described in the inset of Figure 9. To verify the course of energy transfer further, the PL decay curves of Ce^{3+} and energy transfer efficiency (η_T) from Ce^{3+} to Mn^{2+} with various Mn^{2+} concentrations are illustrated in Figure S5. By using eq 7, η_{Ce-Mn} can reach 74%, which is higher than η_{Ce-Tb} (65%) because of the considerable spectral overlap between the emission of Ce^{3+} and the excitation of Mn^{2+}. The remarkable enhancements of the red emission bands compared with the blue emission bands can be observed from experimental data and calculated according to following eqs 9 and 10:[61]

$$W_{decay}^{transfer} = \frac{1}{\tau_{Ce}} - \frac{1}{\tau_{Ce}^{0}} \quad (9)$$

$$\frac{I_R}{I_B} = \frac{W_{Ce-Mn}\gamma_2\tau_2}{\gamma_1} \quad (10)$$

where $\tau_{Ce}{}^0$ and τ_{Ce} are the lifetimes of Ce^{3+} in the absence and presence of Mn^{2+}, respectively; I is the intensity of different emission bands; γ_1 and γ_2 are the radiative transition rates of Ce^{3+} and Mn^{2+} from intrinsic lifetime measurements of 208 ns and 1 ms, respectively, which are independent of Mn^{2+} concentrations; and τ_2 is the lifetime of Mn^{2+} in the presence of Ce^{3+}. Figure 10 shows that the calculated ratios are

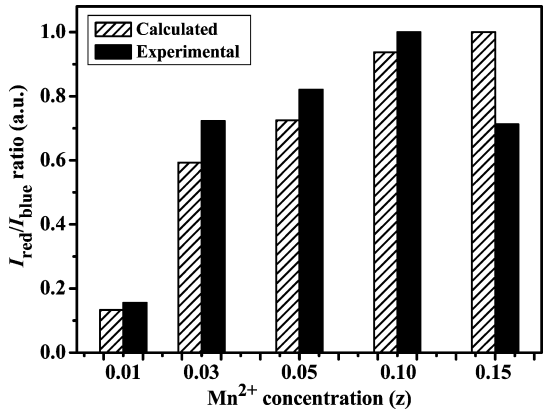

Figure 10. Calculated and experimental ratios I_{red}/I_{blue} (the red band to the blue band) of the $NaSr_{0.99-z}BO_3$:$Ce_{0.01}{}^{3+}$, $Mn_z{}^{2+}$ samples at different Mn^{2+} concentrations. The ratios are scaled to the maximum.

consistent with the intensity ratios obtained directly from the emission spectra in Figure 9, except at z = 0.15. At the maximum Mn^{2+} concentration, a large deviation between the experimental and calculated values of the concentration quenching, reabsorption, and saturation of the energy transfer are found.

3.4. Energy Transfer Rate. Few papers on the relationship between distance and transfer rate of a sensitizer to an activator were found in the literature. The rate determined from the concentration of dopants favorably compares with the result of CIE chromaticity coordinates. The critical distance (R_C) for energy transfer from the Ce^{3+} to Tb^{3+} or Mn^{2+} ions can be calculated. According to Blasse, the critical distance can be expressed by eq 11:[58]

$$R_c \approx 2\left[\frac{3V}{4\pi\chi_c N}\right]^{1/3} \quad (11)$$

where V is the volume of one elementary cell, χ_c is the critical concentration at which the luminescence intensity of sensitizer (Ce^{3+}) is half of that without an activator (Tb^{3+} or Mn^{2+}), and N is the number of substituent sites for the dopant in the unit cell. Hence, the critical distance (R_c) for the energy transfer from the Ce^{3+} to Tb^{3+} or Mn^{2+} ions is about 12.08 and 15.22 Å, respectively. The critical distance between the sensitizer and activator should be shorter than 4 Å for the exchange interaction to result in a resonant energy-transfer mechanism.[62] Given the random distribution of all dopants, the average separation from the sensitizers to the activators can be estimated using eq 12:[61]

$$R_{S-A} = \left(\frac{3V_0}{4\pi NP} \times 1000\right)^{1/3} \quad (12)$$

Equation 12 is similar to eq 11 except that P is the total atomic percent of the two dopants. The rate of energy transfer in the case of electric dipole−quadrupole (dq) can be expressed based on the spatial separation of dopants using eq 13:[61]

$$W = \frac{1}{\tau_S}\left(\frac{R_0}{R_{S-A}}\right)^8 \quad (13)$$

where τ_S is the lifetime of the sensitizer (Ce^{3+}) without an activator (Tb^{3+} or Mn^{2+}); R_0 and R_{S-A} are the critical distance and the spatial separation between the sensitizer and the activator, respectively. The transfer rates of the two series of samples are calculated using eqs 9 and 12, and the results are given in Figure 11. The tendency of the $NaSr_{0.99-y}BO_3:Ce_{0.01}{}^{3+}$, $Tb_y{}^{3+}$ phosphors is close to the dotted curve exhibited by eq 13, and the transfer rate protrudes less than ∼13 Å, which is near the critical distance (R_c = 12.08 Å; Figure 11a). The large deviation (blue line) between the experimental data and the calculated curve of the $NaSr_{0.99-z}BO_3:Ce_{0.01}{}^{3+}$, $Mn_z{}^{2+}$ phosphors may be ascribed to concentration quenching, reabsorption, and saturation of the energy transfer as well as complex interactions that slow the rate of energy transfer (Figure 11b).

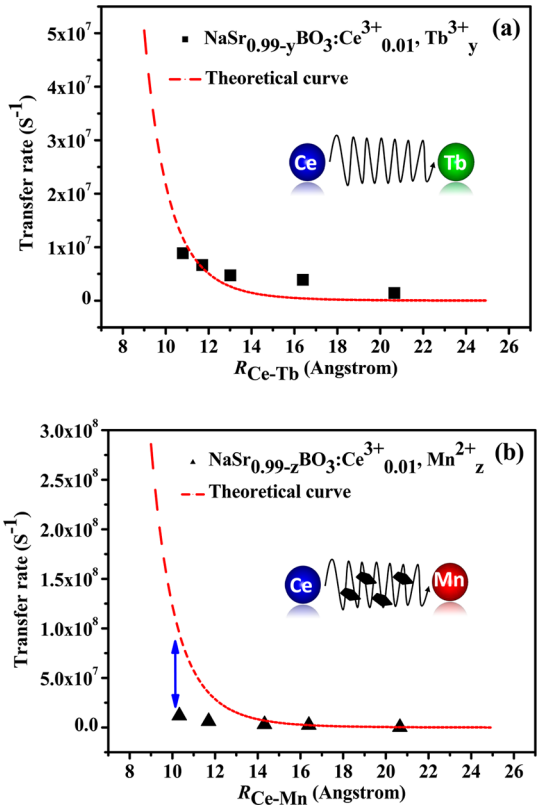

Figure 11. Transfer rates of the (a) $NaSr_{0.99-y}BO_3:Ce_{0.01}{}^{3+}$, $Tb_y{}^{3+}$ and (b) $NaSr_{0.99-z}BO_3:Ce_{0.01}{}^{3+}$, $Mn_z{}^{2+}$ phosphors. The dotted curve shows the calculation using eq 13. The inset shows the process of energy transfer between sensitizer and activator whether obstruction exists or not.

3.5. Mechanism of Electron Transition. This section explores the possible mechanism of electron transition in the $NaSrBO_3:Ce^{3+}$ and $NaSrBO_3:Eu^{2+}$ systems. The density of state spectrum of the $NaSrBO_3:Ce^{3+}$ compound is shown in Figure 12a. The highest occupied state in the Ce doping system is the Ce 4f obital, which is about 2.9 eV lower than the conduction band (CB) edge of the matrix. The splitting of the Ce 4f obitals in the band gap comes from the local-symmetry breaking on the Ce site caused by removal of nearby Na atoms [Figure S6a]. In the CB, the 5d orbitals of Ce are separated by a wider energy range because of the hybridization of the Sr 5s and O 3s states. The 3.1 eV separation between the Ce 5d main peaks and the occupied Ce 4f obital corresponds to the wavelength at 400 nm. This result is similar to the measured emission wavelength of 422 nm in the $NaSrBO_3:Ce^{3+}$ system. In the Eu-doping system, the top of the occupied states is approximately 1.2 eV lower than the CB. The bottom of the Eu 5d obitals is about 0.8 eV higher than the CB edge. This result leads to ionization of the excited 5d electrons because of the overlap between the 5d obitals and the CB edge in the $NaSrBO_3:Eu^{2+}$ system. Furthermore, the few contributions of 5d obitals is observed in Figure 12b. Based on the results mentioned, the absence of the $NaSrBO_3:Eu^{2+}$ sample can be shown by the combined approach (theoretical calculation−experimental research) for the first time. The PL of the Ce 5d−4f transitions is realized, and the forbidden mechanisms of interatomic energy transfer between the $NaSrBO_3:Ce^{3+}$ and $NaSrBO_3:Eu^{2+}$ systems are also proposed. A summary of the luminescence dynamics and energy transfer processes from $Ce^{3+} \rightarrow Tb^{3+}$ or $Ce^{3+} \rightarrow Mn^{2+}$ in the $NaSrBO_3$ host is shown in Figure 13. The Ce^{3+} ion can be used as a sensitizer that transfers its energy via resonance to the activators Tb^{3+} or Mn^{2+}. First, the electrons on Ce^{3+} ions are excited from the ground state (4f) to the excited state (5d) using 365 nm UV light. Subsequently, these electrons relax to the lowest excited state of the 5d orbitals through multiphonon relaxation and then either return to the ground state to produce the Ce^{3+} emissions (5d → $^2F_{5/2}$, $^2F_{7/2}$) or transfer their excitation energy from the stable 5d level to the higher excited energy levels of Tb^{3+} ($^5D_3$) through dipole−quadrupole (dq) interaction followed by relaxation to the $^5D_4$ level to produce green emissions (f−f transition). Third, the red emission is the spin-forbidden $^4T_1(^4G) \rightarrow {}^6A_1(^6S)$ transition of Mn^{2+} attributed to the migration of excited Ce^{3+} electrons to the 3d level of Mn^{2+} via energy transfer, wherein the dipole−quadrupole (dq) interaction occurs again.

3.6. Device. Energy transfer from the sensitizer to the activator is a feasible route to realize color-tunable emission; white-light emission can be obtained by mixing the tricolor (RGB) light sources at a suitable ratio. Figure S7 shows the digital images of the presynthesized samples excited by 365 nm radiation. The excitation spectra of the blue-emitting $NaSrBO_3:Ce$ phosphor is encouraged congruously with a UV chip (λ_{max} = 365 nm). To evaluate the applicability of the borate phosphors, we fabricated three LED devices which consist of the $NaSr_{0.99}BO_3:Ce_{0.01}{}^{3+}$, $NaSr_{0.92}BO_3:Ce_{0.01}{}^{3+}$, $Tb_{0.07}{}^{3+}$, and $NaSr_{0.89}BO_3:Ce_{0.01}{}^{3+}$, $Tb_{0.07}{}^{3+}$, $Mn_{0.03}{}^{2+}$ phosphors and an InGaN chip covered with translucent resin (Figure 14). The CIE chromaticity coordinates calculated from the emission spectra of $NaSrBO_3:Ce^{3+}$; $NaSrBO_3:Ce^{3+}$, Tb^{3+}; and $NaSrBO_3:Ce^{3+}$, Tb^{3+}, Mn^{2+} phosphors are (0.1660, 0.0639), (0.2942, 0.3485), and (0.2810, 0.2505), respectively. The actual PL efficacies of the three devices are 31, 70, and 36 lmW^{-1}, respectively (Figure 14a−c). In addition, Figure S8 displays electroluminescence spectra of $NaSr_{0.89}BO_3:Ce_{0.01}{}^{3+}$, $Tb_{0.07}{}^{3+}$, $Mn_{0.03}{}^{2+}$ which was excited with an InGaN LED (λ_{max} = 365 nm) under different forward bias currents in the range of 10

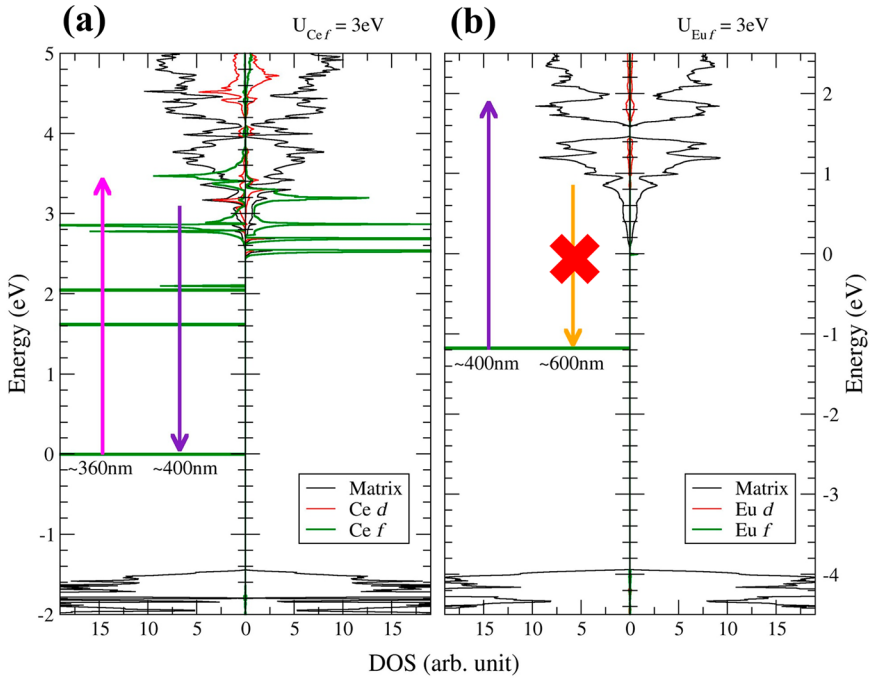

Figure 12. Density of state for the $NaSrBO_3$ with (a) 6.25% Ce-doping and (b) 6.25% Eu-doping systems. All are given by GGA+*U* calculation.

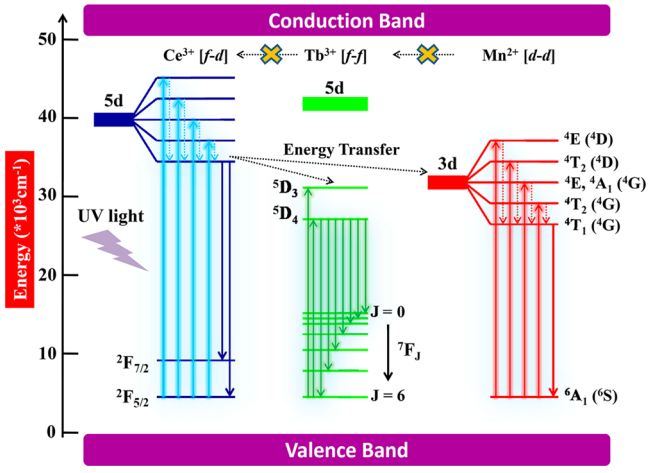

Figure 13. Scheme of energy-level and energy-transfer pathways in $NaSrBO_3$:Ce^{3+}, Tb^{3+}, Mn^{2+}.

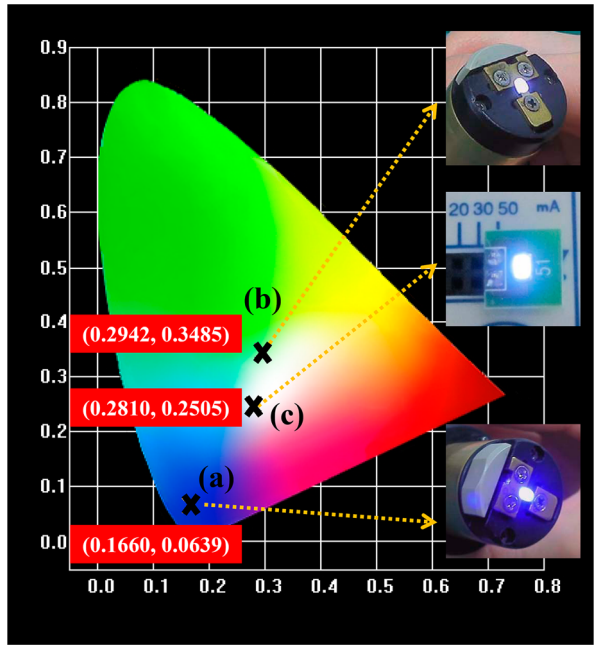

Figure 14. Representation of the CIE chromaticity coordinates for (a) $NaSr_{0.99}BO_3:Ce_{0.01}^{3+}$; (b) $NaSr_{0.92}BO_3:Ce_{0.01}^{3+}$, $Tb_{0.07}^{3+}$; and (c) $NaSr_{0.89}BO_3:Ce_{0.01}^{3+}$, $Tb_{0.07}^{3+}$, $Mn_{0.03}^{2+}$ phosphors. The insets show these devices under a 20 mA forward bias current.

mA to 60 mA. The optical properties of specific component phosphor are also summarized in Table S1. These values are lower than that of a commercial YAG:Ce-based blue chip device based on the complex interaction of the energy transfer, which is ascribed to several factors, such as the reabsorption, large Stokes shift, and nonoptimization. However, the tunable CIE and CCT are obtained by adjusting the components of single-composition white-emitting phosphor ($NaSrBO_3$) in practical applications and performance.

3.7. Comparison $NaSrBO_3$:RE (RE = Ce^{3+}, Tb^{3+}, Mn^{2+}) Phosphors with $NaCaBO_3$:RE (RE = Ce^{3+}, Tb^{3+}, Mn^{2+})[35] Phosphors. Figure 15 presents the effect of alkaline-earth metals (M = Sr, Ca) on PL spectra of the fired $NaMBO_3$:Ce (0.01 atom %) phosphors. The highest PL emission intensity of the $NaSrBO_3$:Ce compound is higher than that of the $NaCaBO_3$:Ce about 31%. Furthermore, the QEs of $NaSrBO_3$:Ce and $NaCaBO_3$:Ce are 85% and 74%, respectively. It is evidence for great effect on the Ce^{3+}–Tb^{3+}/Ce^{3+}–Mn^{2+} energy transfer in a single-composition white-emitting phosphor. The QYs of NSB:Ce^{3+}, Tb^{3+}; NSB:Ce^{3+}, Mn^{2+}; and NSB:Ce^{3+}, Tb^{3+}, Mn^{2+} samples under UV excitation are summarized in Table S2. In addition, the $NaSrBO_3$:Ce is more suitable for application in a commercial UV chip-based device as a result of excited positions. Upon variation of the component, there is a clear change in the shape of PL spectra. The true colors of $NaSrBO_3$:Ce and $NaCaBO_3$:Ce are blue and indigo, respectively (digital photograph is shown as an inset). Thermal properties of luminescent materials are pivotal parameters

dx.doi.org/10.1021/am501232y | ACS Appl. Mater. Interfaces 2014, 6, 9160–9172

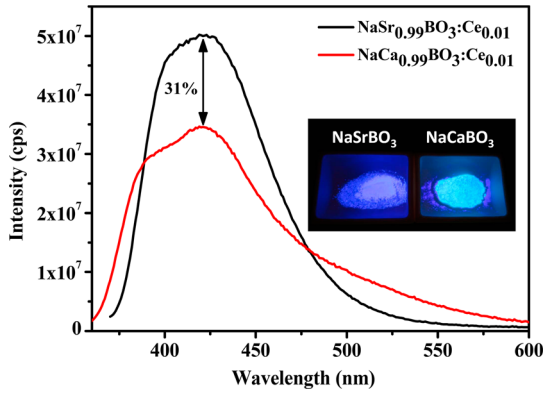

Figure 15. PL spectra of $NaSrBO_3$:Ce and $NaCaBO_3$:Ce (Ce = 0.01 atom %) samples measured at 298 K under 360 and 347 nm excitation, respectively. The inset shows the digital photos of $NaSrBO_3$:Ce and $NaCaBO_3$:Ce samples under 365 nm UV lamp excitation.

which determine the efficiency and reliability of practical devices. According to the definitions, thermal stability of phosphors usually refers to the remaining PL intensity at 150 °C with respect to that at RT. As shown in Figure 16a,b, the decreasing rate of PL intensity is quicker in the $NaCaBO_3$:Ce than that of $NaSrBO_3$:Ce. It means that the $NaSrBO_3$:Ce sample is thermally stable. The thermal quenching behavior of photoluminescence is evaluated by measuring the spectrum of a sample that is heated from ambient temperature to 573 K. The empirical equation: $I_T/I_0 = [1 + D\ \exp(-E_a/kT)]^{-1}$ has been used to fit the curve in Figure 16c, where I_0 (intensity at $T = 0$), D (constant), and E_a (activation energy) are refined variables.[63] $NaSrBO_3$:Ce material has an excellent activation energy (E_a) of ~0.35 eV, which is 1.35 times higher than that of the $NaCaBO_3$:Ce compound (~0.26 eV). Due to the nonradiative transition, the probability of the $NaSrBO_3$:Ce material markedly decreased with a further increase of temperature. The corresponding CIE color coordinates have been calculated from their emission spectra (λ_{ex} = 360, 347 nm) at various temperatures (298−573 K) which have been shown in Figure 16d. It indicates that the $NaSrBO_3$:Ce is blessed with high color purity. In addition, the thermal behavior of the NSB:Ce^{3+}, Tb^{3+}; NSB:Ce^{3+}, Mn^{2+}; and NSB:Ce^{3+}, Tb^{3+}, Mn^{2+} samples is measured as a function of various temperatures (K), as shown in Figure S9. On the basis of the above discussion, the $NaSrBO_3$:Ce, Tb, Mn phosphors have superior properties as compared with $NaCaBO_3$:Ce, Tb, Mn,[35] which lead to real applications as phosphors excited by UV-LEDs to emit white light.

4. CONCLUSIONS

White-emitting, single-composition phosphors with appropriate output efficiency (70 lmW^{-1}), high PL stability, and relatively low price were fabricated using $NaSrBO_3$:RE (RE = Ce^{3+}, Tb^{3+}, Mn^{2+}) compounds. The spectra, decay time, time-resolved PL, and formulas were based on a resonant type mechanism of energy transfer that occurs via a dipole−quadrupole reaction. The accurate measurement of the transfer rate between the Ce^{3+} and Tb^{3+} ions may establish a method to estimate the critical distance of codopants in other luminescent materials. Tuning of the color ratio (I_{Mn}/I_{Ce}) can be obtained simultaneously from calculation of the lifetime and experimental data. The mechanism of luminescence in the

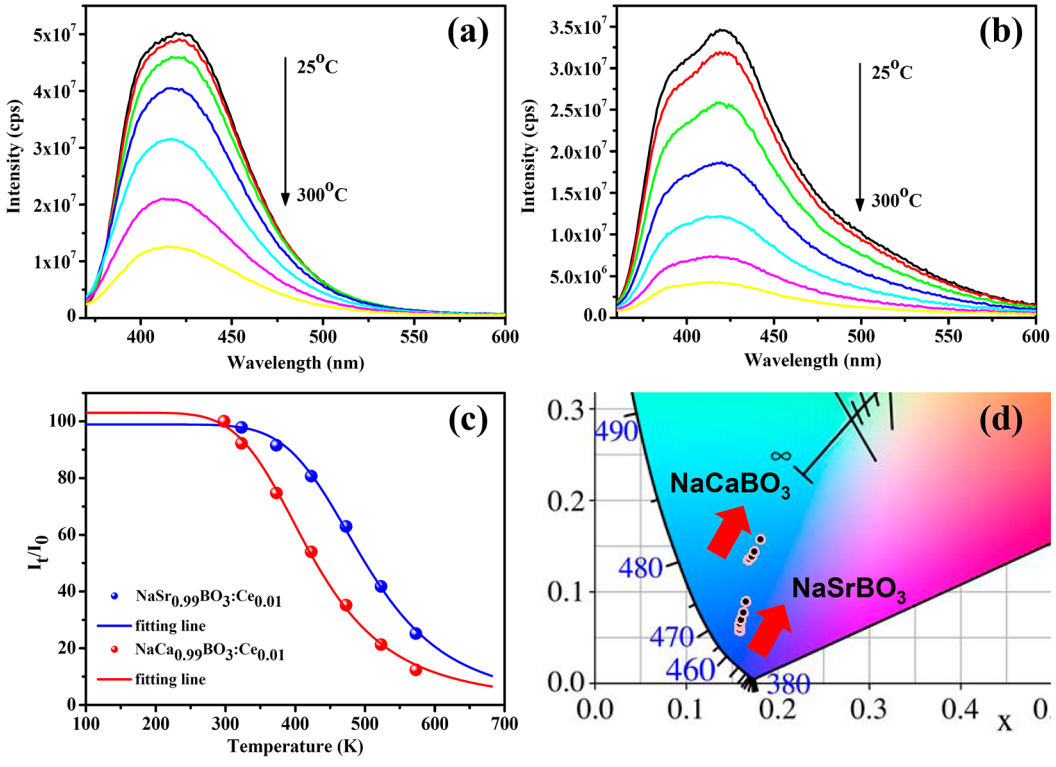

Figure 16. PL emission spectra of (a) $NaSrBO_3$:Ce and (b) $NaCaBO_3$:Ce (Ce = 0.01 atom %) samples measured at various temperatures under 360 and 347 nm excitation, respectively. (c) Integrated blue PL intensity due to the f−d transition as a function of temperature (298−573 K) for the $NaMBO_3$ materials (M = Sr, Ca). (d) CIE color coordinate program of $NaSrBO_3$:Ce (λ_{ex} = 360 nm) and $NaCaBO_3$:Ce (λ_{ex} = 347 nm) samples from 298 to 573 K.

$NaSrBO_3:Eu^{2+}$ system has not been reported in detail until now. We elucidated the band structure and possible mechanism of electron transition to confirm that the 5d−4f transition cannot be generated by theoretical calculation. According to the practical package, the borate phosphors are excellent candidates for UV radiation-excited devices.

■ ASSOCIATED CONTENT

Supporting Information

Computational geometries; digital images; and supporting figures showing additional PL, reflectance spectra, lifetime, and time-resolved PL data are available free of charge via the Internet at http://pubs.acs.org.

■ AUTHOR INFORMATION

Corresponding Author

*E-mail: rsliu@ntu.edu.tw.

Notes

The authors declare no competing financial interest.

■ ACKNOWLEDGMENTS

The authors thank the Ministry of Science and Technology of Taiwan (Contract No. MOST 101-2113-M-002-014-MY3) for financially supporting this research.

■ REFERENCES

(1) Blasse, G.; Bril, A. A New Phosphor for Flying-Spot Cathode-Ray Tubes for Color Television: Yellow-Emitting $Y_3Al_5O_{12}$-Ce^{3+}. *Appl. Phys. Lett.* **1967**, *11*, 53−1−3.

(2) Blasse, G.; Bril, A. Activated Phosphors. *J. Chem. Phys.* **1967**, *47*, 5139−1−7.

(3) Shimizu, Y.; Sakano, K.; Noguchi, Y.; Moriguchi, T. Light Emitting Device Having A Nitride Compound Semiconductor and A Phosphor Containing A Garnet Fluorescent Material. U.S. Patent, US5998925A, 1996.

(4) Jang, H. S.; Yang, H.; Kim, S. W.; Han, J. Y.; Lee, S.-G.; Jeon, D. Y. White Light-Emitting Diodes with Excellent Color Rendering Based on Organically Capped CdSe Quantum Dots and $Sr_3SiO_5:Ce^{3+}$, Li^+ phosphors. *Adv. Mater.* **2008**, *20*, 2696−2702.

(5) Matyba, P.; Yamaquchi, H.; Chhowalla, M.; Robinson, N. D.; Edman, L. Flexible and Metal-Free Light-Emitting Electrochemical Cells Based on Graphene and PEDOT-PSS as the Electrode Materials. *ACS Nano* **2011**, *5*, 574−580.

(6) Inoue, K.; Hirosaki, N.; Xie, R. J.; Takeda, T. Highly Efficient and Thermally Stable Blue-Emitting $AlN:Eu^{2+}$ Phosphor for Ultraviolet White Light-Emitting Diodes. *J. Phys. Chem. C* **2009**, *113*, 9392−9397.

(7) Jang, H. S.; Im, W. B.; Lee, D. C.; Jeon, D. Y.; Kim, S. S. Enhancement of Red Spectral Emission Intensity of $Y_3Al_5O_{12}:Ce^{3+}$ Phosphor Via Pr Co-Doping and Tb Substitution for the Application to White LEDs. *J. Lumin.* **2007**, *126*, 371−377.

(8) Chen, Y.; Gong, M.; Wang, G.; Su, Q. High Efficient and Low Color-Temperature White Light-Emitting Diodes with $Tb_3Al_5O_{12}:Ce^{3+}$ phosphor. *Appl. Phys. Lett.* **2007**, *91*, 071117−1−3.

(9) Mueller-Mach, R.; Mueller, G.; Krames, M. R.; Höppe, H. A.; Stadler, F.; Schnick, W.; Jüstel, T.; Schmidt, P. Highly Efficient All-Nitride Phosphor-Converted White Light Emitting Diode. *Phys. Status Solidi A* **2005**, *202*, 1727−1732.

(10) Piao, X. Q.; Horikawa, T.; Hanzawa, H.; Machida, K. Characterization and Luminescence Properties of $Sr_2Si_5N_8:Eu^{2+}$ Phosphor for White Light-Emitting-Diode Illumination. *Appl. Phys. Lett.* **2006**, *88*, 161908−1−3.

(11) Blasse, G.; Grabmaier, B. C. *Luminescent Materials*; Springer-Verlag: Berlin, 1994; Chapters 4−5.

(12) Jung, K. Y.; Lee, H. W.; Kang, Y. C.; Park, S. B.; Yang, Y. S. Luminescent Properties of (Ba, Sr) $MgAl_{10}O_{17}$:Mn, Eu Green Phosphor Prepared by Spray Pyrolysis under VUV Excitation. *Chem. Mater.* **2005**, *17*, 2729−2734.

(13) Kwon, K. H.; Im, W. B.; Jang, H. S. Luminescence Properties and Energy Transfer of Site-Sensitive $Ca_{6-x-y}Mg_{x-z}(PO_4)_4:Eu_y^{2+},Mn_z^{2+}$ Phosphors and Their Application to Near-UV LED-Based White LEDs. *Inorg. Chem.* **2009**, *48*, 11525−11532.

(14) Kim, J. S.; Jeon, P. E.; Choi, J. C. Warm-White-Light Emitting Diode Utilizing a Single-Phase Full-Color $Ba_3MgSi_2O_8:Eu^{2+},Mn^{2+}$ Phosphor. *Appl. Phys. Lett.* **2004**, *84*, 2931−1−3.

(15) Yu, J.; Guo, C. F.; Ren, Z. Y.; Bai, J. T. Photoluminescence of Double-Color-Emitting Phosphor $Ca_5(PO_4)_3Cl:Eu^{2+}$, Mn^{2+} for Near-UV LED. *Opt. Laser Technol.* **2011**, *43*, 762−766.

(16) Guo, C.; Luan, L.; Ding, X.; Zhang, F.; Shi, F. G.; Gao, F.; Liang, L. Luminescent Properties of $Sr_5(PO_4)_3$ $Cl:Eu^{2+}$, Mn^{2+} as a Potential Phosphor for UV-LED-Based White LEDs. *Appl. Phys. B: Laser Opt.* **2009**, *95*, 779−785.

(17) Suriyamurthy, N.; Panigrahi, B. S. Luminescence of $BaAl_2O_4:Mn^{2+},Ce^{3+}$ Phosphor. *J. Lumin.* **2007**, *127*, 483−488.

(18) Zhang, X. G.; Zhou, L. Y.; Gong, M. L. Luminescence Properties of Dual-Emission Ce^{3+}, Mn^{2+} Doped $NaSrBO_3$ Phosphors. *ECS J. Solid State Sci. Technol.* **2013**, *2*, R83−R86.

(19) Sun, J. F.; Lian, Z. P.; Shen, G. Q.; Shen, D. Z. Blue-White-Orange Color-Tunable Luminescence of Ce^{3+}/Mn^{2+}-Codoped $NaCaBO_3$ via Energy Transfer: Potential Single-Phase White-Light-Emitting Phosphors. *RSC Adv.* **2013**, *3*, 18395−18405.

(20) Liu, W. R.; Chen, T. M. Single-Phased White-Light Phosphors $Ca_9Gd(PO_4)_7:Eu^{2+},Mn^{2+}$ under Near-Ultraviolet Excitation. *J. Phys. Chem. C* **2010**, *114*, 18698−18701.

(21) Yu, M.; Lin, J.; Zhou, Y. H.; Wang, S. B.; Zhang, H. J. Sol-Gel Deposition and Luminescent Properties of Oxyapatite $Ca_2(Y,Gd)_8(SiO_4)_6O_2$ Phosphor Films Doped with Rare Earth and Lead Ions. *J. Mater. Chem.* **2002**, *12*, 86−91.

(22) Hsu, C. H.; Lu, C. H. Microwave-Hydrothermally Synthesized $(Sr_{1-x-y}Ce_xTb_y)Si_2O_{2-\delta}N_{2+\mu}$ Phosphors: Efficient Energy Transfer, Structural Refinement and Photoluminescence Properties. *J. Mater. Chem.* **2011**, *21*, 2932−2939.

(23) Huang, C. H.; Luo, L. Y.; Chen, T. M. An Investigation on the Luminescence and $Ce^{3+} \rightarrow Eu^{2+}$ Energy Transfer in $Ca_9Y(PO_4)_7:Ce^{3+},Eu^{2+}$ Phosphor. *J. Electrochem. Soc.* **2011**, *158*, J341−J344.

(24) Xia, Z. G.; Liu, R. S. Tunable Blue-Green Color Emission and Energy Transfer of $Ca_2Al_3O_6F:Ce^{3+},Tb^{3+}$ Phosphors for Near-UV White LEDs. *J. Phys. Chem. C* **2012**, *116*, 15604−15609.

(25) Shang, M. M.; Li, G. G.; Kang, X. J.; Yang, D. M.; Geng, D. L.; Lin, J. Tunable Luminescence and Energy Transfer Properties of $Sr_3AlO_4F:RE^{3+}$ (RE = Tm/Tb, Eu, Ce) Phosphors. *ACS Appl. Mater. Interfaces* **2011**, *3*, 2738−2746.

(26) Geng, D. L.; Li, G. G.; Shang, M. M.; Yang, D. M.; Zhang, Y.; Cheng, Z. Y.; Lin, J. Color Tuning via Energy Transfer in $Sr_3In(PO_4)_3:Ce^{3+}/Tb^{3+}/Mn^{2+}$ Phosphors. *J. Mater. Chem.* **2012**, *22*, 14262−14271.

(27) Li, G. G.; Geng, D. L.; Shang, M. M.; Peng, C.; Cheng, Z. Y.; Lin, J. Tunable Luminescence of Ce^{3+}/Mn^{2+}-Coactivated $Ca_2Gd_8(SiO_4)_6O_2$ Through Energy Transfer and Modulation of Excitation: Potential Single-Phase White/Yellow-Emitting Phosphors. *J. Mater. Chem.* **2011**, *21*, 13334−13344.

(28) Dexter, D. L. A Theory of Sensitized Luminescence in Solids. *J. Chem. Phys.* **1953**, *21*, 836−1−15.

(29) Ye, S.; Liu, Z. S.; Wang, J. G.; Jing, X. P. Luminescent Properties of $Sr_2P_2O_7$:Eu,Mn Phosphor under Near UV Excitation. *Mater. Res. Bull.* **2008**, *43*, 1057−1065.

(30) Wu, L.; Chen, X. L.; Zhang, Y.; Kong, Y. F.; Xu, J. J.; Xu, Y. P. Ab Initio Structure Determination of Novel Borate $NaSrBO_3$. *J. Solid State Chem.* **2006**, *179*, 1219−1224.

(31) Liu, W. R.; Huang, C. H.; Wu, C. P.; Chiu, Y. C.; Yeh, Y. T.; Chen, T. M. High Efficiency and High Color Purity Blue-Emitting $NaSrBO_3:Ce^{3+}$ Phosphor for Near-UV Light-Emitting Diodes. *J. Mater. Chem.* **2011**, *21*, 6869−6874.

(32) Yang, F.; Liang, Y. J.; Liu, M. Y.; Li, X. J.; Zhang, M. F.; Wang, N. Photoluminescence Properties of Novel Red-Emitting NaSr-

BO_3:Eu^{3+} Phosphor for Near-UV Light-Emitting Diodes. *Opt. Laser Technol.* **2013**, *46*, 14−19.
(33) Yang, F.; Liang, Y. J.; Lan, Y. Z.; Gao, W. J.; Liu, M. Y.; Li, X. J.; Huang, W. Z.; Li, Y. L.; Xia, Z. G. A Novel Green-Emitting Phosphor $NaSrBO_3$:Tb^{3+}, Li^+. *Mater. Lett.* **2012**, *83*, 59−61.
(34) Kumar, V.; Bedyal, A. K.; Pitale, S. S.; Ntwaeaborwa, O. M.; Swart, H. C. Synthesis, Spectral and Surface Investigation of $NaSrBO_3$:Sm^{3+} Phosphor for Full Color Down Conversion in LEDs. *J. Alloys Compd.* **2013**, *554*, 214−220.
(35) Zhang, X. G.; Gong, M. L. Single-Phased White-Light-Emitting $NaCaBO_3$:Ce^{3+}, Tb^{3+}, Mn^{2+} Phosphors for LED Applications. *Dalton Trans.* **2014**, *43*, 2465−2472.
(36) Zhang, X. G.; Song, J. H.; Zhou, C. Y.; Zhou, L. Y.; Gong, M. L. High Efficiency and Broad Band Blue-Emitting $NaCaBO_3$:Ce^{3+} Phosphor for NUV Light-Emitting Diodes. *J. Lumin.* **2014**, *149*, 69−74.
(37) Larson, C.; Von Dreele, R. B. *Generalized Structure Analysis System (GSAS), Los Alamos National Laboratory Report LAUR 86−748*; Los Alamos National Laboratory: Los Alamos, NM, 1994.
(38) Momma, K.; Izumi, F. VESTA: A Three-Dimensional Visualization System for Electronic and Structural Analysis. *J. Appl. Crystallogr.* **2008**, *41*, 653−658.
(39) Blöchl, P. E. Projector Augmented-Wave Method. *Phys. Rev. B* **1994**, *50*, 17953−17979.
(40) Anisimov, V. I.; Solovyev, I. V.; Korotin, M. A.; Czyzyk, M. T.; Sawatzky, G. A. Density-Functional Theory and NiO Photoemission Spectra. *Phys. Rev. B* **1993**, *48*, 16929−16934.
(41) Kresse, G.; Hafner, J. Ab Initio Molecular Dynamics for Open-Shell Transition Metals. *Phys. Rev. B* **1993**, *48*, 13115−13118.
(42) Kresse, G.; Furthmüller, J. Efficiency of Ab-Initio Total Energy Calculations for Metals and Semiconductors Using a Plane-Wave Basis Set. *Comput. Mater. Sci.* **1996**, *6*, 15−50.
(43) Shannon, R. D. Revised Effective Ionic Radii and Systematic Studies of Interatomic Distances in Halides and Chalcogenides. *Acta Crystallogr., Sect. A* **1976**, *32*, 751−767.
(44) Guo, N.; Song, Y. H.; You, H. P.; Jia, G.; Yang, M.; Liu, K.; Zheng, Y. H.; Huang, Y. J.; Zhang, H. J. Optical Properties and Energy Transfer of $NaCaPO_4$:Ce^{3+},Tb^{3+} Phosphors for Potential Application in Light-Emitting Diodes. *Eur. J. Inorg. Chem.* **2010**, *29*, 4636−4642.
(45) van Krevel, J. W. H.; Hintzen, H. T.; Metselaar, R.; Meijerink, A. Long Wavelength Ce^{3+} Emission in Y-Si-O-N Materials. *J. Alloys Compd.* **1998**, *268*, 272−277.
(46) Dorenbos, P. The 5d Level Positions of the Trivalent Lanthanides in Inorganic Compounds. *J. Lumin.* **2000**, *91*, 155−176.
(47) Judd, B. R. Optical Absorption Intensities of Rare Earth Ions. *Phys. Rev.* **1962**, *127*, 750−761.
(48) Ofelt, G. S. Intensities of Crystal Spectra of Rare-Earth Ions. *J. Chem. Phys.* **1962**, *37*, 511−1−10.
(49) Gruber, J. B.; Bahram, Z.; Reid, M. F. Spectra, Energy Levels, and Transition Line Strengths for Sm^{3+}:$Y_3Al_5O_{12}$. *Phys. Rev.* **1999**, *60*, 15643−15653.
(50) May, P. S.; Metcalf, D. H.; Richardson, F. S.; Carter, R. C.; Miller, C. E. Measurement and Analysis of Excited-state Decay Kinetics and Chiroptical Activity in the $^6H_J \leftarrow {}^4G_{5/2}$ Transitions of Samarium(3+) in Trigonal $Na_3[Sm(C_4H_4O_5)_3]\cdot{}_2NaClO_4\cdot 6H_2O$. *J. Lumin.* **1992**, *51*, 249−268.
(51) Quan, Z. W.; Wang, Z. L.; Yang, P. P.; Lin, J.; Fang, J. Y. Synthesis and Characterization of High-Quality ZnS, ZnS:Mn^{2+}, and ZnS:Mn^{2+}/ZnS (Core/Shell) Luminescent Nanocrystals. *Inorg. Chem.* **2007**, *46*, 1354−1360.
(52) Shi, L.; Huang, Y. L.; Seo, H. J. Emission Red Shift and Unusual Band Narrowing of Mn^{2+} in $NaCaPO_4$ Phosphor. *J. Phys. Chem. A* **2010**, *114*, 6927−6934.
(53) Orgel, L. E. Spectra of Transition-Metal Complexes. *J. Chem. Phys.* **1955**, *23*, 1004−1−11.
(54) Tanner, P. A.; Mak, C. S. K.; Edelstein, N. M.; Murdoch, K. M.; Liu, G.; Huang, J.; Seijo, L.; Barandiaran, Z. Absorption and Emission Spectra of Ce^{3+} in Elpasolite Lattices. *J. Am. Chem. Soc.* **2003**, *125*, 13225−13233.
(55) Dorenbos, P. Relating the Energy of the [Xe]5d1 Configuration of Ce^{3+} in Inorganic Compounds with Anion Polarizability and Cation Electronegativity. *Phys. Rev. B* **2002**, *65*, 235110−1−6.
(56) Tallant, D. R.; Miller, M. P.; Wright, J. C. Energy Transfer and Relaxation Phenomena in Erbium(3+)-Doped Calcium Fluoride. *J. Chem. Phys.* **1976**, *65*, 510−1−12.
(57) Miller, M. P.; Wright, J. C. Multiphonon and Energy Transfer Relaxation in Charge-Compensated Crystals. *J. Chem. Phys.* **1979**, *71*, 324−1−15.
(58) Blasse, G. Energy Transfer in Oxidic Phosphors. *Philips Res. Rep.* **1969**, *24*, 131−144.
(59) Paulose, P. I.; Jose, G.; Thomas, V.; Unnikrishnan, N. V.; Warrier, M. K. R. Sensitized Fluorescence of Ce^{3+}/Mn^{2+} System in Phosphate Glass. *J. Phys. Chem. Solids* **2003**, *64*, 841−846.
(60) Reisfeld, R.; Lieblich-Soffer, N. Energy Transfer from Uranyl(2+) to Samarium(3+) in Phosphate Glass. *J. Solid State Chem.* **1979**, *28*, 391−396.
(61) Powell, R. C. *Physics of Solid-State Laser Materials*; Springer-Verlag: New York, 1998; Chapters 7.
(62) Antipeuko, B. M.; Bataev, I. M.; Ermolaev, V. L.; Lyubimov, E. I.; Privalova, T. A. Ion-to-Ion radiationless Transfer of Electron Excitation Energy Between Rare-Earth Ions in $POCl_3$-$SnCl_4$. *Opt. Spectrosc.* **1970**, *29*, 177−180.
(63) Lin, C. C.; Shen, C.-C.; Liu, R.-S. Spiral-Type Heteropolyhedral Coordination Network Based on Single-Crystal $LiSrPO_4$: Implications for Luminescent Materials. *Chem.—Eur. J.* **2013**, *19*, 15358−15365.